Science Press

ARTICLE

Arc Erosion Behavior and Mechanism of CuCr25 Cathode Material in Different Ambient Atmospheres

Wang Lili,   Feng Yi,   Cao Mengli,   Zhao Ting,   Zhou Zijue,   Zhao Hao

School of Materials Science and Engineering, Hefei University of Technology, Hefei 230009, China

Abstract: The arc erosion behavior of CuCr25 cathode material in oxygen, argon, and carbon dioxide atmospheres under voltage of 9 kV was studied. The arc duration and arc energy are decreased with changing the atmosphere in the order of oxygen, argon, and carbon dioxide, whereas the variation trend of breakdown strength is opposite. The erosion morphologies of molten pools, bulges, holes, splashes, and cracks formed on the CuCr25 material surface under the high temperature and high energy of the arc were analyzed by scanning electron microscope and three-dimensional laser scanning confocal microscope. The results indicate that the most severe erosion occurs in oxygen atmosphere and the slightest erosion occurs in carbon dioxide atmosphere, which can be attributed to the differences in arc energy. According to the results of X-ray photoelectron spectroscopy analysis, the oxidation reactions in oxygen and carbon dioxide atmospheres produce CuO, Cr_2O_3, and CrO_3, while no new compounds are formed in argon atmosphere.

Key words: CuCr25 cathode material; arc erosion; different atmospheres

The electrical contact material has wide applications in the industry fields, because it is the core component of the electrical switch to connect/break the circuit and bear the current[1]. Arc discharge occurs between the electrical contacts during the usage of switch device. The high temperature and high energy of the arc leads to the erosion on surface of electric contact materials, resulting in surface deformation or material loss and shortening the service life of materials[2,3]. Therefore, the electric contact materials require the good mechanical properties, stable chemical properties, and good electrical/thermal conductivity, especially the high arc erosion resistance[4,5].

Currently, the arc erosion performance of Cu-based materials attracts much attention due to their wide applications under medium and high voltage load situations[6-8]. The CuCr materials have been widely investigated because of their excellent comprehensive properties, such as higher voltage resistance, fine damage resistance, and excellent breaking property[9]. The arc erosion resistance of CuCr materials also has been widely studied. Rieder et al[10] found that the fine Cr particles can reduce the

maximum chopper current of CuCr materials, and the breakdown voltage significantly increases. Guan et al[11] compared the arc erosion behavior of CuCr10, CuCr25, and CuCr50 materials, and found that the discharge uniformity is increased with increasing the Cr content. The typical uniform erosion morphology of CuCr50 alloy can be attributed to the synergistic effect of the Cr oxide and the uniform distribution of Cr phase. Yang et al[12] studied the motion of vacuum arc spots of nanocrystalline and coarse-grained CuCr25 materials. It is found that the movement of arc spots on Cr particles of coarse-grained CuCr25 material is random, while that on nanocrystalline CuCr25 material abides by the sub-directional arrangement, which may be related to the internal electric field of CuCr materials. Cao et al[13] found that the Mo addition causes the variation of the first breakdown phase from Cr phase to Cu phase in CuCr50 material, leading to the splitting and migration of the cathode spot, which greatly reduces the concentrated erosion and improves the arc erosion resistance of materials.

However, few studies discuss the effect of the environment atmosphere on CuCr materials. The effect of ambient

atmosphere on arc erosion performance of electrical contact materials mainly includes two aspects. Firstly, the effect of ambient atmosphere on arc energy and arc duration should be investigated, which directly reflect the arc extinguishing ability of the gas. Secondly, the effect of chemical reactions between the atmosphere and the materials should be studied. Some new compounds generated during the chemical reactions may affect the anti-arc erosion performance of materials[14,15]. With the development trend of miniaturization, large capacity, and long service life of the relay system, it is more and more important to improve the anti-arc erosion performance of electrical contact materials.

In this research, the erosion behavior of CuCr25 material prepared by hot-pressing sintering method was studied in oxygen, argon, and carbon dioxide atmospheres at voltage of 9 kV. The morphologies and composition of the erosion surface were analyzed. The erosion mechanism of CuCr25 material in different ambient atmospheres was discussed.

1 Experiment

The Cr powder (purity≥99.99%, particle size of 45 μm, Xing Rongyuan Technology Co., Ltd) and the electrolytic Cu powder (purity≥99.99%, particle size of 38 μm) were mixed in a vacuum ball mill with the ball-to-material ratio of 10:1. The argon was filled as the protective gas, and the anhydrous ethanol was added as the dispersant. The mixed powder was ball-milled at 50 r/min for 10 h with standing interval of 20 min per hour. The well-mixed powders were then loaded into the round graphite mold with diameter of 45 μm. The CuCr25 specimens were prepared in the hot-pressing sintering furnace at 1020 °C for 1.5 h under the pressure of 30 MPa. The argon gas was used as the protective atmosphere throughout the sintering process. After the furnace-cooling to room temperature, the specimens were taken out and cut into small blocks for subsequent tests.

The relative density of the CuCr25 material can be calculated by Eq.(1), as follows:

$$\Delta = \frac{\rho}{\rho_0} \times 100\% \tag{1}$$

where ρ is the actual density of specimens and ρ_0 is the theoretical density. The actual density can be measured by Archimedes method and the theoretical density can be calculated by Eq.(2), as follows:

$$\rho_0 = \sum_1^n \rho_i \varphi_i = \rho_1 \varphi_1 + \rho_2 \varphi_2 \tag{2}$$

where ρ_1 is the density of Cu; φ_1 is the volume fraction of Cu; ρ_2 is the density of Cr; φ_2 is the volume fraction of Cr.

The Brinell hardness of CuCr25 material was tested by the Brinell hardness tester (HBV-30A). The pressure head was a quenched steel ball with diameter D=1 mm, the load was 10 kg, and the pressure holding time was 30 s. The value of Brinell hardness (HB) was obtained by Eq.(3), as follows:

$$HB = \frac{0.102P}{A} = \frac{0.204P}{\pi D (D - \sqrt{D^2 - d^2})} \tag{3}$$

where P is the applied load (kg), A is the indentation area (mm^2), D is the diameter of steel ball (mm), and d is the

diameter of the circular indentation (mm). Five points were measured for each specimen, and their average measurement was used as the Brinell hardness of the materials.

The flexural strength of CuCr25 material was measured by the three-point bending method through the Shimadzu universal material testing machine (DCS-5000). The distance of the support endpoint was 30 mm, and the loading rate was 0.5 mm/min. Each specimen was tested for three times, and the average value was used as the obtained strength. The strength of CuCr25 material was calculated by Eq. (4), as follows:

$$\sigma_b = \frac{3FL}{2bh^2} \tag{4}$$

where σ_b is the flexural strength of CuCr25 material (N/mm^2), F is the maximum flexural force of the specimen before fracture (N), L is the distance of the support endpoint (mm), b is the width of the specimen (mm), and h is the height of the specimen (mm).

The two-arm electric bridge instrument was used to measure the conductivity of the specimen, which can be expressed by Eq.(5), as follows:

$$\sigma = \frac{IL}{US} \tag{5}$$

where σ is the conductivity of the specimen (MS/m), U is the voltage between two electric potential needles (mV), I is the current through the specimen (A), S is the cross-sectional area of the specimen (mm^2), and L is the distance between two electric potential needles (mm). The specimens conducted different currents, and the conductivity of the CuCr25 material was obtained.

The CuCr25 specimen after hot-pressing sintering was cut into the cathode specimens with the size of 10 mm×10 mm×3 mm by wire cutting. The tungsten rod was served as the anode with a small cylinder tip with diameter of 2 mm. The specimen was placed above the tungsten anode and the voltage of 9 kV was loaded between the cathode and the anode. The experiment simulated the arc discharge process in different atmospheres, including the oxygen, argon, and carbon dioxide. The vacuum pump was used to vacuum the closed chamber, and then the designed gas was injected into the closed chamber. The cathode specimen was controlled by an automatic stepping machine to move slowly to the anode until the arc was discharged. The digital storage oscilloscope (ADS1102 CAL) was used to record the parameters and waveform of the whole discharge process. The surface morphology of the eroded specimen was observed by field emission scanning electron microscopy (FE-SEM, SU8020). Three-dimensional morphologies were observed, and relevant data were measured by the three-dimensional laser scanning confocal microscope (3D LSCM, VK-X250, KEYENCE). The element composition of the eroded surface was analyzed by energy dispersive X-ray spectrometer (EDS) and the chemical composition was analyzed by X-ray photoelectron spectroscope (XPS). The X-ray diffraction (XRD) was also used for analysis.

2 Results

2.1 Physical and mechanical properties of CuCr25 cathode materials

FE-SEM surface morphology of the polished CuCr25 cathode material is shown in Fig. 1a. The light area is Cu-rich phase, while the dark area is the Cr-rich phase. The Cr particles are uniformly distributed in the Cu matrix. Fig. 1b shows XRD patterns of the mixed powder, ball-milled powder, and sintered specimen of the CuCr25 material. According to the Cu-Cr binary phase diagram[16], the mutual solubility between Cu and Cr is very small, so these two elements are in the form of pseudo alloys in CuCr25 materials[17,18]. It can be seen from Fig. 1b that only Cu and Cr phases can be detected, indicating that no impurity is introduced and no new phase is formed. According to Table 1, the diffraction peaks of Cu and Cr of different forms in CuCr15 material are basically the same, and the lattice constants of Cu and Cr barely change as well. This phenomenon indicates that Cr is not solid-solvated into Cu during ball milling or sintering to form the solid solution, i.e., the amount of solid solution Cr into Cu is too small to influence the Cu lattice constant, inferring that the amount of solid solution Cr can be neglected[19-21].

Table 2 shows the results of physical and mechanical properties of CuCr25 material. The relative density of the CuCr25 specimen reaches 99.1%, indicating that the hot-pressing sintering process parameters are suitable. Meanwhile, the presence of Cr particles significantly improves the mechanical strength and Brinell hardness of CuCr25 material, but inevitably leads to the decline in electrical conductivity.

2.2 Arc discharge behavior of CuCr25 cathode materials in different atmospheres

The arc discharge parameters recorded by the oscilloscope in the arc erosion tests under the voltage of 9 kV are presented in Fig. 2. In Fig. 2, the current marked by the red arrow represents the breakdown current, i. e., when the gas decomposes, the arc begins to discharge. Then, the current is decreased rapidly to the critical current, which corresponds to the arc duration marked by the black arrow in Fig. 2. The critical arc duration of the current has an important influence on the erosion behavior of cathode materials. Generally, the arc duration reflects the ability of the arc extinguishing of gas. Table 3 shows the arc parameters during the arc discharge process in different atmospheres. According to Table 3, the difference in breakdown current in different atmospheres is small. The arc duration in oxygen atmosphere is the longest of 32.7 ms, while that in carbon dioxide atmosphere is the shortest of 30.14 ms.

The arc energy is an important electrical parameter of the arc. In general, the greater the arc energy, the more serious the
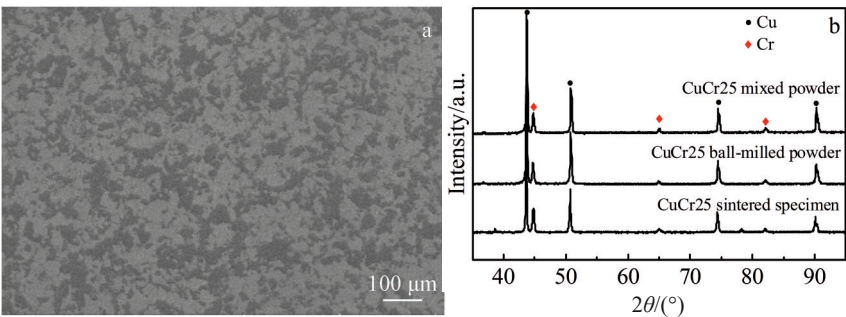

Fig.1   FE-SEM surface morphology of polished CuCr25 cathode material (a); XRD patterns of mixed powder, ball-milled powder, and sintered specimen of CuCr25 cathode material (b)

Table 1   Diffraction angles and lattice constants of Cu and Cr in CuCr25 material under different conditions

CuCr25 material form	2θ/(°)		Lattice constant/nm	
	Cu (111)	Cr (110)	Cu	Cr
Mixed powder	43.3425	44.3929	0.3613	0.2882
Ball-milled powder	43.3163	44.3630	0.3616	0.2885
Sintered specimen	43.3416	44.3666	0.3614	0.2884

Table 2   Physical and mechanical properties of CuCr25 specimens

Relative density/%	Brinell hardness, HB/MPa	Flexural strength/MPa	Electrical conductivity/ MS·m^{-1}
99.1	981.0	454	30.8

erosion of the material. The arc energy W can be calculated by Eq.(6), as follows:

$$W=UIt \tag{6}$$

where U represents the load voltage between the cathode and the anode (kV), I represents the breakdown current (A), and t represents the arc duration (ms). According to Table 3, the arc energy and the arc duration are both decreased with changing the atmosphere in the order of oxygen, argon, and carbon dioxide.

The breakdown strength indicates the maximum electric field strength that materials can withstand without being damaged. The higher the breakdown strength, the more difficult the arc generation between two electrodes. The breakdown strength can be calculated by Eq.(7), as follows:
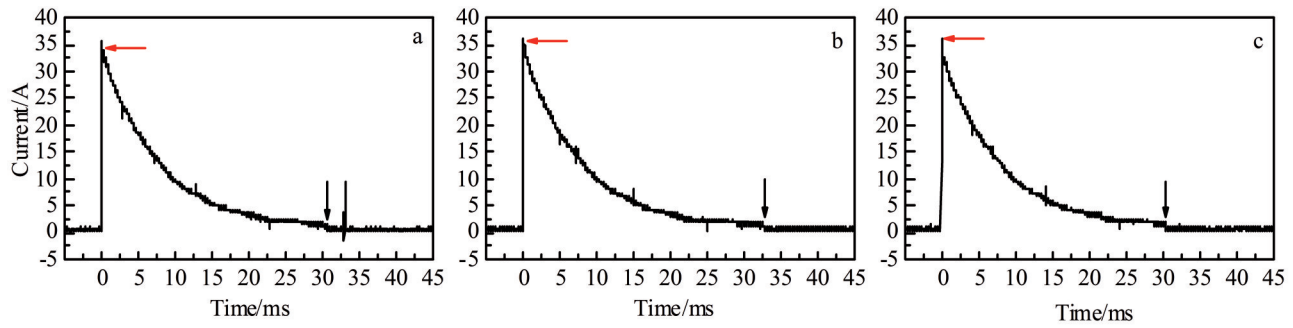
$$E=U/d \tag{7}$$

Fig.2　Current-time curves of CuCr25 cathode materials under voltage of 9 kV in different atmospheres: (a) oxygen, (b) argon, and (c) carbon dioxide

Table 3　Arc parameters in different atmospheres

Parameter	Oxygen	Argon	Carbon dioxide
Breakdown current/A	36.07	35.63	36.06
Arc duration/ms	32.70	31.07	30.14
Arc energy/J	10 615	9 963	9 781
Breakdown strength/×10⁶ V·m⁻¹	0.69	1.01	1.11

where E is the breakdown strength (V/m), U is the load voltage (V), and d is the distance between the cathode and the anode during the arc discharge (m). The variation trend of breakdown strength in different atmospheres is opposite to

that of the arc duration and arc energy. The breakdown strength in oxygen is the lowest of 0.69×10^6 V/m and that in carbon dioxide is the highest of 1.11×10^6 V/m.

2.3 Three-dimensional morphologies of CuCr25 cathode materials in different atmospheres

The erosion morphologies of CuCr25 materials in different atmospheres are reconstructed by 3D LSCM, as shown in Fig. 3. In Fig. $3a_1 \sim 3c_1$, the red areas represent the bump structure and the black areas represent pits or holes. When the arc is generated, the resultant temperature (up to 5000 K[22]) is much higher than the melting point of Cu and Cr, leading to
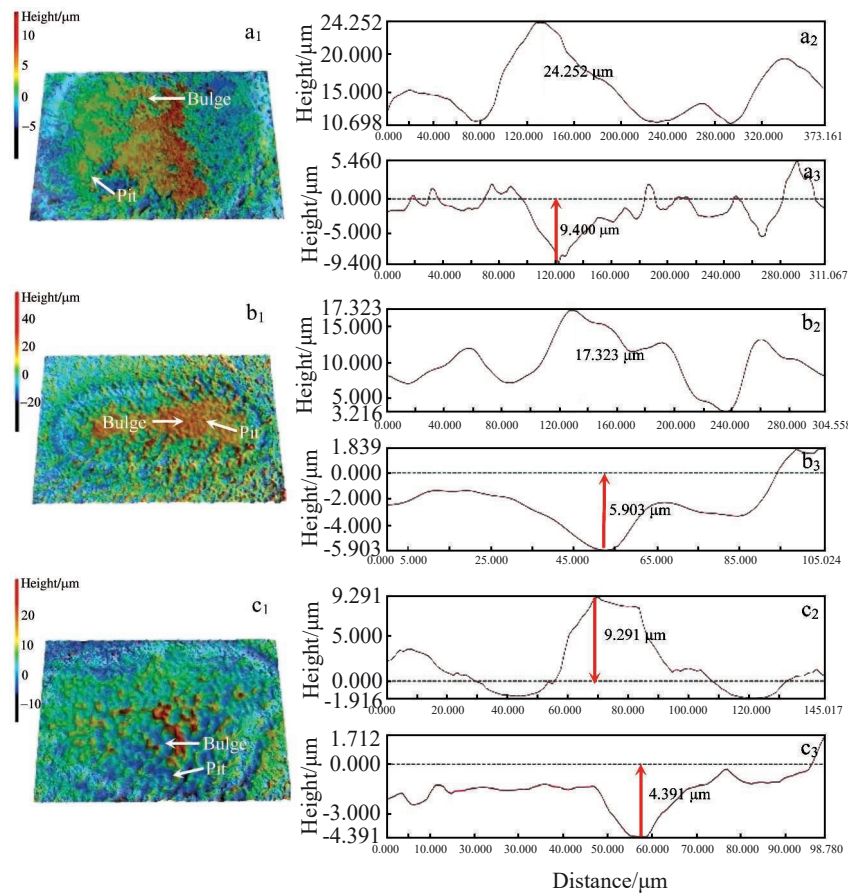

Fig.3　3D erosion morphologies ($a_1 \sim c_1$), bulge heights ($a_2 \sim c_2$), and pit depths ($a_3 \sim c_3$) of CuCr25 cathode materials in oxygen ($a_1 \sim a_3$), argon ($b_1 \sim b_3$), and carbon dioxide ($c_1 \sim c_3$) atmospheres

the formation of molten pools on the surface of CuCr25 materials. Under the electromagnetic stirring, the molten pool flows from the center to edge, and then the bulge structure is formed after cooling. Meanwhile, under the high-energy impact of the arc, the liquid metal in the molten pool splashes outward, which produces splash particles and results in pits and holes in the molten pool. As shown in Fig.3, the erosion surfaces in different atmospheres all have bulge and pit structures. The number of bulges is decreased gradually with changing the atmosphere in the order of oxygen, argon, and carbon dioxide. This phenomenon is related to the difference of arc energy in different atmospheres. The higher the arc energy, the higher the temperature of molten pool and the stronger the electromagnetic stirring effect, i.e., more bulges are generated by the pushing force.

The height of bulges and the depth of pits are also measured by the lines marked in Fig.3a$_1$~3c$_1$. It can be seen that the bulge height of the erosion surface in oxygen, argon, and carbon dioxide atmospheres is 24.252, 17.323, and 9.291 μm, respectively, presenting the decreasing trend. Fig.3a$_3$~3c$_3$ show the pit depths of the erosion surface in oxygen, argon,

and carbon dioxide atmospheres, which are 9.400, 5.903, and 4.391 μm, respectively. The results indicate that the arc energy significantly affects the erosion morphology of the material surface, and the higher the arc energy, the more serious the erosion.

2.4 Microstructure and composition of CuCr25 cathode materials after arc erosion under different atmospheres

2.4.1 Oxygen atmosphere

The erosion morphologies of the CuCr25 cathode materials in oxygen atmosphere are shown in Fig.4. Numerous bulges and holes of 3~5 μm in diameter on the erosion surface can be observed. Fig.4b shows the morphology of erosion edge. Plenty of spherical particles appear at the erosion edge, indicating that a large amount of splashing occurs in the molten pool during the arc discharge. Some extended cracks can also be observed at the erosion edge. EDS point scanning was conducted on the particles marked by black crosses in Fig.4b. The results show that the average mass ratio of Cu:Cr= 2.74, which is lower than the original mass ratio of Cu:Cr=3.0 in CuCr25 materials, indicating that both Cu and Cr splash
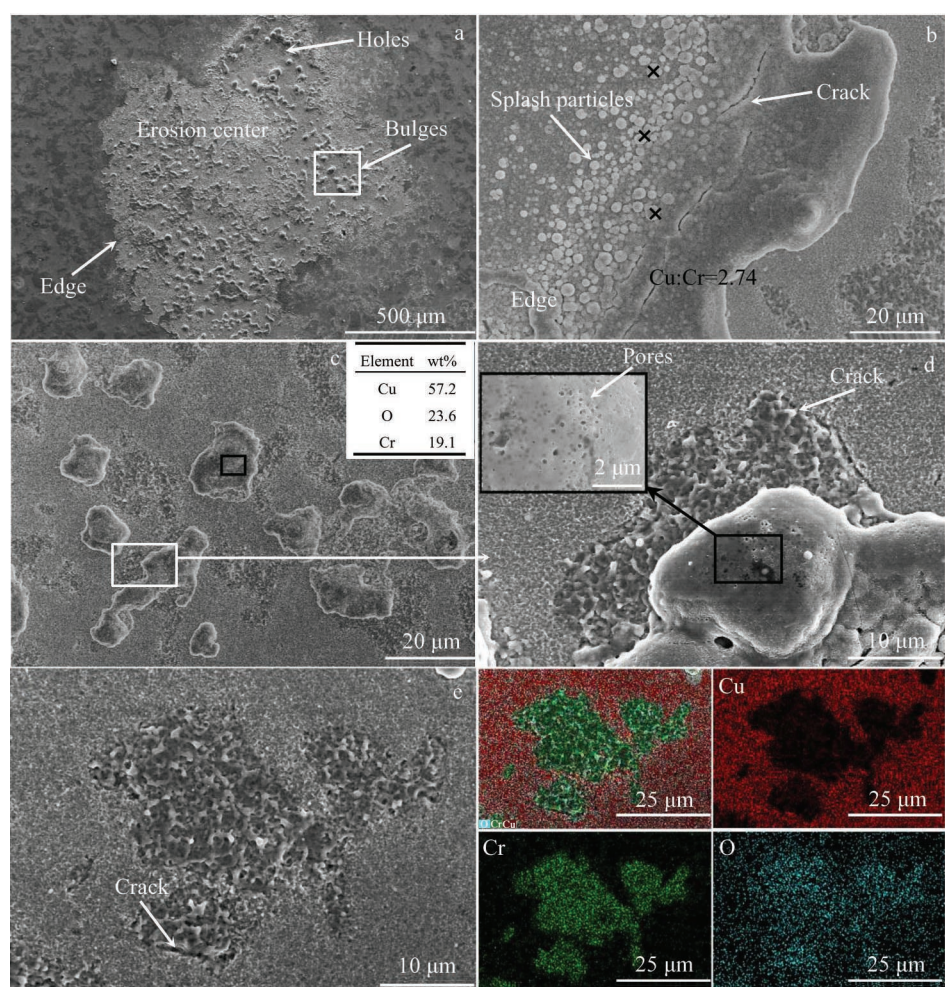

Fig.4　Erosion morphologies of CuCr25 cathode material in oxygen atmosphere: (a) overall morphology; (b) erosion edge morphology; (c) magnified image of white rectangle area in Fig.4a and EDS results of bulge; (d) magnified image of white rectangle area in Fig.4c; (e) shallow erosion pit; (f) corresponding EDS element distributions of Fig.4e

under the high arc energy and the Cr splash is more than the Cu splash.

Fig.4c is the magnified image of the white rectangle area in Fig. 4a. The bulge morphology in the erosion center can be observed. EDS point scanning results show that the bulge contains Cu, Cr, and O elements, indicating that lots of O_2 is dissolved in the molten pool during the formation process of bulges. The numerous pores on the bulge surface (Fig.4d) are caused by the escape of a large amount of supersaturated gas after the arc disappears and the temperature drops[23].

In addition to bulges, some heavily eroded shallow pits are scattered on the erosion surface, which are composed of eroded Cr particles, and the surrounding flat area is the Cu matrix. The uniform distribution of O element indicates that the surface is oxidized after erosion. It can be observed that the erosion of Cr is more serious than that of Cu. The extended cracks appear at the interface of Cu and Cr, as shown in Fig.4d and 4e, which are caused by the difference in thermal expansion coefficients of Cu and Cr, resulting in the stress concentration.

The surface chemical composition of CuCr25 cathode material after arc erosion in oxygen atmosphere was also analyzed by XPS. As shown in Fig. 5a, four peaks of Cu 2p spectra can be observed. Two main peaks at 934.6 and 953.7 eV are related to Cu $2p_{3/2}$ and Cu $2p_{1/2}$ peaks of CuO[24,25], respectively. Meanwhile, CuO can also be determined by the satellite peaks of Cu $2p_{3/2}$ and Cu $2p_{1/2}$ peaks at 944.08 and 962.68 eV[26-28], respectively. Fig.5b shows XPS spectra of Cr 2p. The two main peaks at 579.2 and 588.4 eV correspond to Cr $2p_{3/2}$ and Cr $2p_{1/2}$ orbits, respectively, which are obtained by the peak fitting of Cr $2p_{3/2}$ region. The peaks at 579.2 and 576.7 eV correspond to CrO_3[29] and Cr_2O_3[30], respectively, indicating that Cr^{3+} and Cr^{6+} coexist on the erosion surface of CuCr25 specimen. This is because the oxygen content in this experiment is high, and the temperature of the erosion center increases sharply in arc discharge. Thus, partial Cr^{3+} is further oxidized into Cr^{6+}. According to XPS analyses, the surface of CuCr25 specimen is oxidized after arc erosion in oxygen atmosphere, and the products are CuO, CrO_3, and Cr_2O_3.

2.4.2 Argon atmosphere

The small size bulges and erosion holes form on the erosion surface in argon atmosphere, as shown in Fig. 6a. Compared

with that in oxygen atmosphere, the size of splash particles in argon atmosphere (Fig. 6b) is much smaller due to the lower arc energy. Based on EDS point scanning results of splash particles marked by the black crosses in Fig.6b, the mass ratio of Cu:Cr=2.37, which is also lower than the original mass ratio. At the erosion center marked by the white rectangle area in Fig.6a, the erosion of Cr particles is more serious than that of Cu matrix, and the splash particles generated in the molten pool form the bump structure of different sizes. In addition, the cracks at the interface of Cu and Cr induced by stress concentration can also be observed, as shown in Fig. 6b and 6c. The stacking particles can be observed in Fig. 6d, which may be due to the aggregation of splash particles and the rapid solidification prior to melting.

EDS analysis results of stacking particles show that the bulge is composed of only Cu and Cr elements. Therefore, no other compounds are generated during arc discharge in argon atmosphere.

2.4.3 Carbon dioxide atmosphere

Fig.7a shows the overall erosion morphology of the CuCr25 material in carbon dioxide atmosphere: only bulges without obvious erosion holes can be observed. Due to the lowest arc energy of arc discharge in carbon dioxide atmosphere, the splash in the molten pool is greatly reduced. Thus, a small number of particles are observed at the erosion edge, as shown in Fig. 7b. EDS point scanning analyses of splash particles marked by black crosses in Fig.7b show that the mass ratio of Cu:Cr=2.48, which is also less than the original mass ratio of 3, indicating that more Cr is splashed.

Fig. 7c shows the morphology of the erosion center. It can be seen that a small number of pores appear on the bulge surface. Since the solubility of the gas is decreased with decreasing the temperature, less gas is dissolved in the molten pool in carbon dioxide atmosphere than that in oxygen atmosphere due to the lower arc energy. Thus, the number of pores caused by gas escape is greatly reduced. According to Fig. 7c and 7d, the bulge is composed of Cu, Cr, and O elements. O element is generated by the decomposition of CO_2 under the high temperature caused by the arc.

The chemical composition of the erosion area is characterized by XPS analysis, as shown in Fig.8. The Cu $2p_{3/2}$ peak (934.88 eV), Cu $2p_{1/2}$ peak (953.7 eV), and their satellite
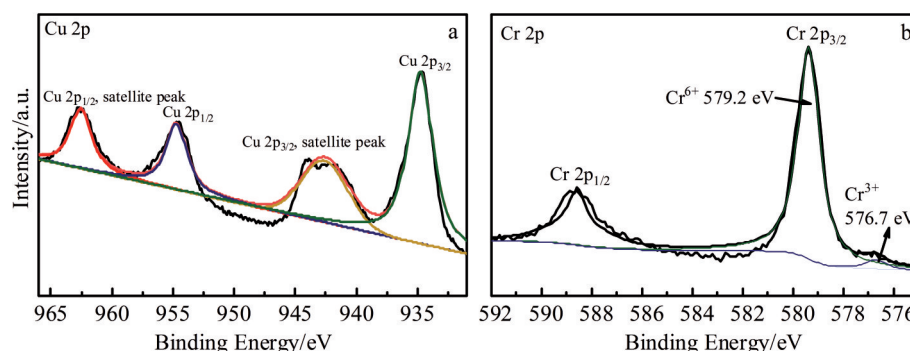

Fig.5   XPS spectra of CuCr25 cathode materials after arc erosion in oxygen atmosphere: (a) Cu 2p and (b) Cr 2p
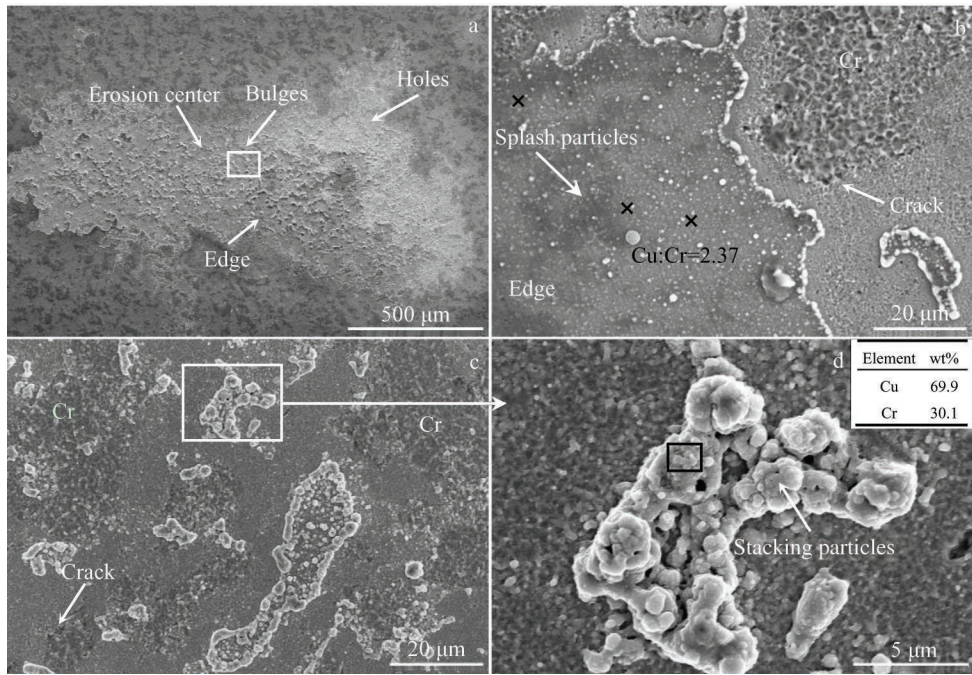
Fig.6   Erosion morphologies of CuCr25 cathode material in argon atmosphere: (a) overall morphology; (b) erosion edge morphology;
(c) magnified image of white rectangle area in Fig.6a; (d) magnified image of white rectangle area in Fig.6c and EDS results
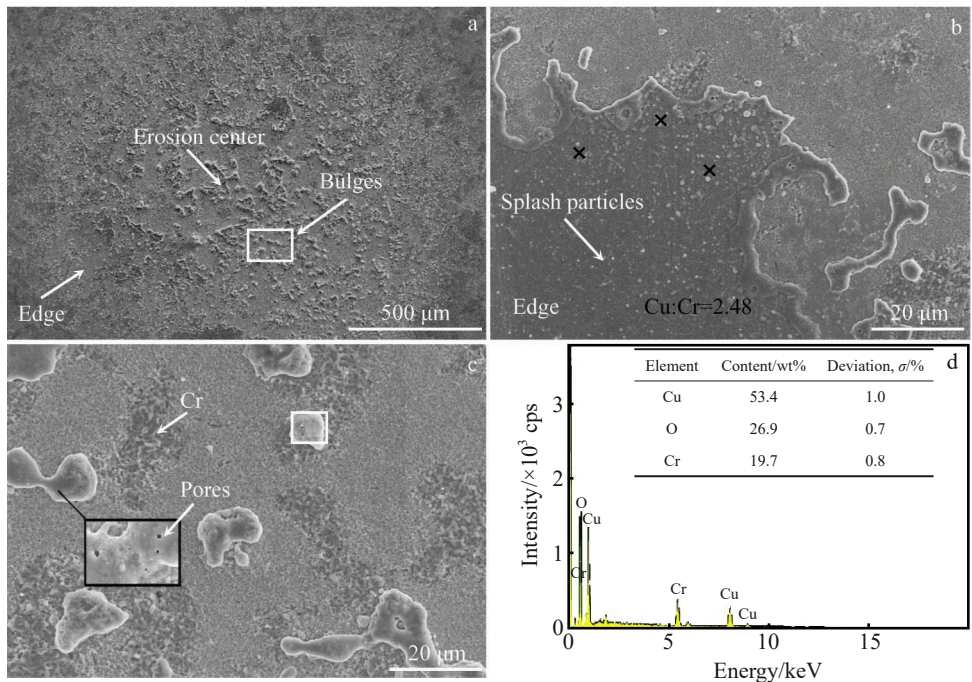of stacking particles on bulge

Fig.7   Erosion morphologies of CuCr25 cathode material in carbon dioxide atmosphere: (a) overall morphology; (b) erosion edge morphology;
(c) magnified image of white rectangle area in Fig.7a; (d) EDS results of white rectangle area in Fig.7c

peaks are all attributed to CuO[24-28]. As shown in Fig.8b, after peak fitting of Cr $2p_{3/2}$ peak (579.5 eV), the peaks at 579.5 and 576.9 eV correspond to CrO_3[29] and Cr_2O_3[30], respectively. Meanwhile, the satellite peak of Cr $2p_{3/2}$ is obtained by peak fitting at 587.1 eV, which is attributed to Cr_2O_3[31]. The results show that the oxidation products on the surface of CuCr25

material after arc erosion in carbon dioxide atmosphere are CuO, CrO_3, and Cr_2O_3.

3 Discussion

3.1 Arc discharge mechanism

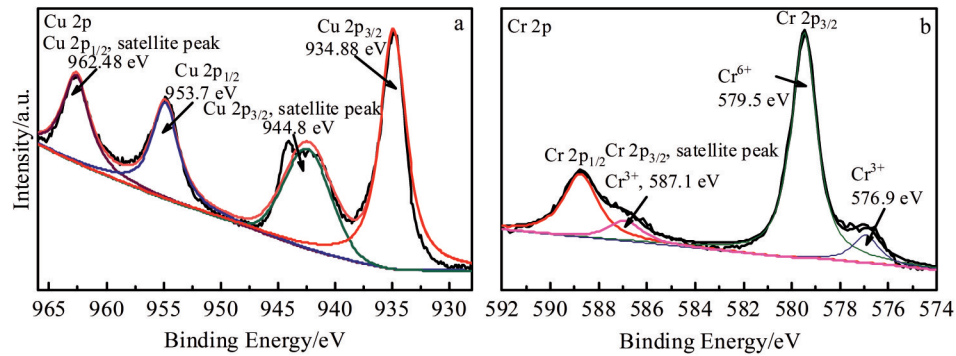Arc is a strong gas discharge phenomenon. Under certain

Fig.8　XPS spectra of CuCr25 cathode material after arc erosion in carbon dioxide atmosphere: (a) Cu 2p and (b) Cr 2p

conditions of voltage and current, when the electric field between two components exceeds a certain value, the electrons on the cathode surface accelerate and form free electrons in space, namely the strong field emission. The free electrons accelerate towards the anode under the electric field force. In this process, the free electrons collide with the neutral particles in the gas repeatedly, which forms numerous free electrons and positive ions. The neutral gas is insulating and non-conductive, but it can conduct electricity with the presence of these charged electron ions. The electric conductivity increases continuously, finally resulting in the breakdown of gas gap and thus producing the arc. After the arc is formed, the high temperature increases the kinetic energy of gas molecules, resulting in the collision ionization to form electrons and positive ions, namely the thermal ionization[32]. In the arc column, the deionization occurs when the electrons and positive ions are compounded into neutral particles or diffused outside the arc column, which is the opposite process of thermal ionization. The thermal ionization and deionization are in equilibrium during the steady arc discharge. When the deionization rate is faster than the thermal ionization rate, the arc will be extinguished[22].

3.2 Erosion mechanism of CuCr25 cathode material in different atmospheres

Due to the high temperature and high arc energy, the erosion surfaces of the CuCr25 cathode material in oxygen, argon, and carbon dioxide atmospheres all present the typical erosion morphologies, such as bulge, pit, molten pool, splash particles, and cracks. Due to the pseudo-alloy structure in CuCr25 material, the phase separation occurs when hot arc plasma is generated on the cold cathode surface[33,34]. Thus, the Cr phase with lower density (Cr: ~6.9 $g \cdot cm^{-3}$; liquid Cu: 8.9 $g \cdot cm^{-3}$) gradually rises to the surface, resulting in the more severe splash of Cr. This is also the reason for the fact that the value of mass ratio of Cu:Cr in splash particles at the erosion edge area is 2.74, 2.37, and 2.48 in oxygen, argon, and carbon dioxide atmospheres, respectively. Ref. [35-37] reported that the breakdown of alloy is different from that of pure metal during arc discharge, because the arc occurs preferentially on the relatively weak phase in the alloy. CuCr25 material is composed of Cu and Cr phases, so the breakdown firstly occurs on Cr particles. Therefore, the erosion of Cr phase is more serious than that of Cu matrix in different atmospheres. When the Cr phase is eroded, the heat is rapidly transferred to the Cu matrix through the Cu/Cr interface[38] due to the good thermal conductivity of Cu.

The schematic diagrams of arc erosion mechanisms of CuCr25 material in different atmospheres are shown in Fig.9. The erosion mechanism of CuCr25 cathode material in oxygen atmosphere is shown in Fig.9a. This process has the longest arc duration and the highest arc energy. The arc preferentially occurs on the Cr phase, and the heat is transferred to the Cu matrix through the Cu/Cr interface. Since the arc temperature is much higher than the melting
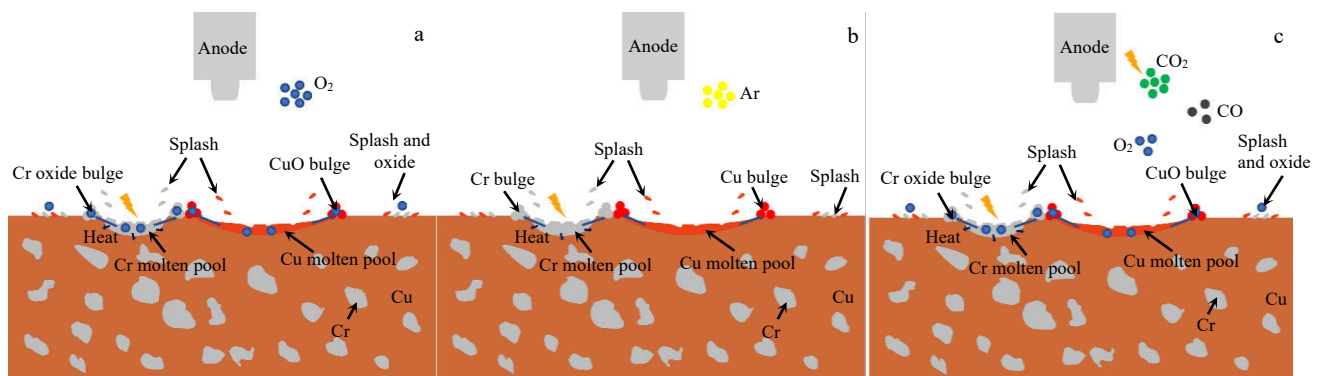

Fig.9　Schematic diagrams of erosion mechanisms of CuCr25 cathode materials in different atmospheres: (a) oxygen, (b) argon, and (c) carbon dioxide

point of Cu and Cr, the molten pool is formed on the material surface. Meanwhile, a large amount of O_2 is dissolved in the molten pool, and then both Cu and Cr are oxidized. The molten pool flows from the center to the edge under the stirring action of the electromagnetic force, and it splashes under the high arc energy. After the arc disappears, the liquid alloy is cooled rapidly and the gas in the molten pool escapes explosively. Therefore, the severe erosion morphology is formed on the CuCr25 cathode material surface in oxygen atmosphere.

The erosion mechanism of CuCr25 cathode material in argon atmosphere is shown in Fig.9b. This process has lower arc energy than that in oxygen atmosphere does. Therefore, the erosion is less severe than that in oxygen atmosphere. As an inert gas, the argon is chemically stable, thereby resulting in less dissolution in the molten pool. Thus, the erosion mechanism in argon atmosphere is relatively simple. Cu and Cr only undergo the phase transformation in the arc process. The molten pools, splash particles, and holes are formed, but no new compounds are generated during the arc discharge.

The erosion mechanism of CuCr25 cathode material in carbon dioxide atmosphere is shown in Fig.9c. CO_2 has weak electron adsorption capacity and is not sensitive to the uniformity of electric field, so it has a certain insulation performance[39]. Meanwhile, CO_2 begins to decompose into CO and O_2 when the temperature is over 2200 K, which absorbs partial energy, resulting in the excellent arc extinguishing performance. The chemical reaction of CO_2 decomposition is as follows:

$$CO_2 \xrightarrow{\text{High temperature}} O_2 + CO \tag{8}$$

The decomposition of CO_2 causes the short arc duration and low arc energy of the arc process in carbon dioxide atmosphere. Therefore, the erosion morphology in carbon dioxide is the least severe. Because of the production of O_2, the subsequent erosion processes are similar to that in oxygen atmosphere. Cu and Cr are oxidized due to the presence of O_2.

4 Conclusions

1) The arc duration and arc energy are increased with changing the atmosphere in the order of carbon dioxide, argon, oxygen. The breakdown strength is decreased with changing the atmosphere in the order of carbon dioxide, argon, oxygen.

2) The erosion morphology is affected by the arc energy. In oxygen atmosphere, the CuCr25 material presents the most severe erosion morphology with the existence of numerous bulges, holes, cracks, and splash particles. In argon atmosphere, the size of bulges is decreased, and less defects can be found. The erosion morphology is the least severe in the carbon dioxide atmosphere with a small number of bulges, splash particles, and pores.

3) In oxygen and carbon dioxide atmospheres, the erosion surface is oxidized with the generation of CuO, CrO_3, and Cr_2O_3. Whereas in argon atmosphere, no new compounds are

formed on the erosion surface.

References

1 He D H, Manory R. *Wear*[J], 2001, 249(7): 626

2 Cui R, Han Y, Zhu Z X *et al. Journal of Alloys and Compounds*[J], 2019, 777: 1159

3 Sun Caixin, Wang Jue, Yan Ping. *High Voltage Apparatus*[J], 2012, 48(1): 82 (in Chinese)

4 Zhou Y J, Song K X, Xing J D. *Acta Metallurgica Sinica (English Letters)*[J], 2016, 29(4): 399

5 Klinski K V, Kowanda C, Heilmaier M *et al. Journal of Alloys and Compounds*[J], 2015, 631: 237

6 Yang X H, Zhao Y P, Kang D D *et al. Engineering Failure Analysis*[J], 2020, 118: 104 865

7 Guo Zhongquan, Geng Haoran, Guo Ying *et al. Electronic Components and Materials*[J], 2009, 28(3): 45 (in Chinese)

8 Qian Gang, Feng Yi, Huang Xiaochen *et al. Rare Metal Materials and Engineering*[J], 2018, 47(6): 1818 (in Chinese)

9 Li Feng, Li Zhinian, Zhong Jingming *et al. Rare Metal Materials and Engineering*[J], 2019, 48(10): 3331 (in Chinese)

10 Rieder W F, Schussek M, Glatzle W *et al. IEEE Transactions on Components, Hybrids, and Manufacturing Technology*[J], 1989, 12(2): 273

11 Guan W M, Yuan J, Lv H *et al. Journal of Materials Science and Technology*[J], 2021, 81: 1

12 Yang Z M, Zhang Q L, Zhang C Y *et al. Physics Letters A*[J], 2005, 353(1): 98

13 Cao W C, Liang S H, Zhang X *et al. Vacuum*[J], 2011, 85(10): 943

14 Xin C, Wu J W, Liu B *et al. IEEE Transactions on Plasma Science*[J], 2014, 42(10): 2722

15 Zhu Qingcheng, Liu Zixun, Liu Wenxuan *et al. High Voltage Apparatus*[J], 2018, 54(9): 6 (in Chinese)

16 Okamoto H. *Journal of Phase Equilibria and Diffusion*[J], 2012, 33(4): 342

17 Vadchenko S G, Suvoroav E V, Mukhina N I *et al. Russian Journal of Nonferrous Metals*[J], 2021, 62(2): 233

18 Chai L J, Zhou Z M, Xiao Z P *et al. Science China Technological Sciences*[J], 2015, 58(3): 462

19 Ungar T. *Scripta Materialia*[J], 2004, 51(8): 777

20 Delhez R, Keijser T H, Mittemeijer E J. *Fresenius Journal of Analytical Chemistry*[J], 1982, 312(1): 1

21 Yang X H, Li X J, Xiao Z *et al. Journal of Alloys and Compounds*[J], 2016, 686: 648

22 Zhao H, Feng Y, Zhou Z J *et al. Journal of the European Ceramic Society*[J], 2021, 41(4): 2263

23 Zhang J S, Teixeira R A, Zhang H M *et al. Analytical Chemistry*[J], 2017, 89(16): 8524

24 Pierrick G, Philippe F, Sophie D *et al. Fuel Processing Technology*[J], 2016, 153: 129

25 Jolley J G, Geesey G G, Haukins M R *et al. Applied Surface*

Science[J], 1989, 37(4): 469

26 Dube C E, Workie B, Kounaves S P *et al. Journal of the Electrochemical Society*[J], 1995, 142(10): 3357

27 Poulston S, Parlett P M, Stone P *et al. Surface and Interface Analysis*[J], 1996, 24(12): 811

28 Ren S M, Cui M J, Pu J B *et al. ACS Applied Materials & Interfaces*[J], 2017, 9(32): 27 152

29 Murphy V, Tofail S A M, Hughes H *et al. Chemical Engineering Journal*[J], 2009, 148(2-3): 425

30 Aleksandra T, Patryk O, Ryszard D. *Environmental Science and Pollution Research*[J], 2015, 22(8): 5985

31 Grohmann I, Kemnitz E, Lippitz A *et al. Surface and Interface Analysis*[J], 1995, 23(13): 887

32 Zhou Z J, Feng Y, Zhao H *et al. Ceramics International*[J], 2021, 47(2): 2319

33 Tepper J, Seeger M, Votteler T *et al. IEEE Transactions on Components and Packaging Technologies*[J], 2006, 29(3): 658

34 Zhu S X, Liu Y, Tian B H *et al. Vacuum*[J], 2017, 143: 129

35 Zhang C Y, Wang Y P, Yang Z M *et al. Acta Metallurgica Sinica* (*English Letters*)[J], 2003, 16(2): 151

36 Ding B J, Yang Z M, Wang X T. *IEEE Transactions on Components, Packaging, and Manufacturing Technology*[J], 1996, 19(1): 76

37 Cao W C, Liang S H, Zhang X *et al. International Journal of Refractory Metals and Hard Materials*[J], 2011, 29(2): 237

38 Duan Wenxin, Guo Conghui, Yang Zhimao *et al. Rare Metal Materials and Engineering*[J], 2005, 34(6): 998 (in Chinese)

39 Zhao H, Li X W, Zhu K *et al. IEEE Transactions on Dielectrics and Electrical Insulation*[J], 2016, 23(5): 2657

CuCr25阴极材料在不同环境气氛下的电弧烧蚀行为及机理

汪丽丽，凤　仪，曹梦丽，赵　霆，周子珏，赵　浩

(合肥工业大学 材料科学与工程学院，安徽 合肥 230009)

摘　要：研究了9 kV电压下CuCr25阴极材料在氧气、氩气和二氧化碳气氛下的电弧烧蚀行为。燃弧时间和电弧能量按照氧气、氩气、二氧化碳的环境气氛变化顺序依次减小，而击穿强度的变化趋势则相反。利用扫描电子显微镜和三维激光共聚焦显微镜分析了在电弧的高温、高能量作用下CuCr25材料表面形成的熔池、凸起、孔洞、飞溅和裂纹等烧蚀形貌。结果表明：CuCr25材料在氧气中烧蚀得最严重，在二氧化碳中电弧烧蚀最轻微，这可能与电弧能量的差异有关。X射线光电子能谱分析结果显示，在氧气和二氧化碳中电弧烧蚀表面发生氧化反应，生成了CuO、CrO_3和Cr_2O_3，而在氩气环境中没有新的化合物形成。

关键词：CuCr25阴极材料；电弧烧蚀；不同气氛

作者简介：汪丽丽，女，1997年生，硕士，合肥工业大学材料科学与工程学院，安徽 合肥 230009，电话：0551-62904715，E-mail：wanglili@mail.hfut.edu.cn